Pulkkinen, T.I.; Dimmock, A.P.; Osmane, A.; Nykyri, K.

Solar wind energy input to the magnetosheath and at the magnetopause

Published in:
Geophysical Research Letters

DOI:
10.1002/2015GL064226

Published: 01/01/2015

Document Version
Publisher's PDF, also known as Version of record

Please cite the original version:
Pulkkinen, T. I., Dimmock, A. P., Osmane, A., & Nykyri, K. (2015). Solar wind energy input to the magnetosheath and at the magnetopause. Geophysical Research Letters, 42(12), 4723-4730.
https://doi.org/10.1002/2015GL064226

AGU PUBLICATIONS

Geophysical Research Letters

RESEARCH LETTER
10.1002/2015GL064226

Key Points:
- Driver at magnetopause is not a direct mapping of solar wind parameters
- High solar wind speed increases magnetospheric energy input efficiency
- High negative IMF Bz decreases magnetospheric energy input efficiency

Correspondence to:
T. I. Pulkkinen,
tuija.pulkkinen@aalto.fi

Citation:
Pulkkinen, T. I., A. P. Dimmock, A. Osmane, and K. Nykyri (2015), Solar wind energy input to the magnetosheath and at the magnetopause, *Geophys. Res. Lett.*, *42*, 4723–4730, doi:10.1002/2015GL064226.

Received 13 APR 2015
Accepted 4 JUN 2015
Accepted article online 6 JUN 2015
Published online 26 JUN 2015

Solar wind energy input to the magnetosheath and at the magnetopause

T. I. Pulkkinen[1], A. P. Dimmock[1], A. Osmane[1], and K. Nykyri[2]

[1]Department of Radio Science and Engineering, Aalto University, Espoo, Finland, [2]Embry-Riddle Aeronautical University, Daytona Beach, Florida, USA

Abstract Using Time History of Events and Macroscale Interactions During Substorms observations, we show that the efficiency of the energy entry through the magnetopause as measured by the Poynting vector normal component depends on the combination of the solar wind speed and the southward component of the interplanetary magnetic field (IMF): Most efficient energy transfer occurs when the IMF B_Z is only moderately negative, and the solar wind speed is high. This means that for the same level of solar wind driver parameters (electric field, epsilon, or other), different combinations of V and B_Z will produce different driving at the magnetopause. The effect is strongest for low to moderate driving conditions, while the influence is smaller for the intense space weather events.

1. Introduction

In a two-dimensional view, the magnetospheric plasma is in a constant motion powered by the merging of the geomagnetic field with the antiparallel component of the interplanetary magnetic field (IMF) [*Dungey*, 1961; *Yeh*, 1976]. At the tailward end, another reconnection process leads to closure of the open field lines which then begin to convect Earthward. During magnetospheric substorms, a new neutral line forms in the midtail region, causing dipolarization of the inner magnetotail field and tailward ejection of plasma behind the X line [*Hones*, 1979]. This global circulation pattern has been verified by numerous satellite observations [e.g., *Cowley*, 1982; *Pudovkin et al.*, 1986; *Nishida et al.*, 1996; *Baker et al.*, 1996; *Kepko et al.*, 2014].

A three-dimensional extension of the Dungey cycle connects the X points at the subsolar point and in the distant magnetotail by a continuous X line that in a due southward IMF case follows the magnetopause at the equatorial plane and connects through the magnetotail along the distant tail X line. For cases when the IMF is oriented at an angle θ from the northward direction, the X line along the magnetopause becomes tilted such that the reconnection line is perpendicular to the vector connecting the magnetic field vectors in the magnetospheric and magnetosheath sides [*Sonnerup*, 1974]. If the field magnitudes are equal in both sides, the X line orientation is given by $\sin(\theta/2)$. Assuming an average magnetospheric field of 70 nT and shock compression ratio of 4, this would require an IMF magnitude of ~17 nT. For more typical weaker IMF values, the *Sonnerup* [1974] model predicts smaller X line tilt than $\sin(\theta/2)$.

Laitinen et al. [2007] examined the orientation of the large-scale X line using the Grand Unified Magnetosphere-Ionosphere Coupling Simulation version 4 (GUMICS-4) global MHD simulation [*Janhunen et al.*, 2012]. They found that the X line was strongly tilted away from the equatorial plane for IMF orientations away from the due southward direction. Possible merging sites were found to be close to the $\sin(\theta/2)$ predicted by the *Sonnerup* [1974] model. *Pulkkinen et al.* [2010] used observations and the GUMICS-4 and Lyon-Fedder-Mobarry [*Lyon et al.*, 2004] global MHD simulations to conclude that the energy entry correlates well with the electric field along the large-scale X line, indicating that the energy transfer process involves the entire magnetopause rather than being dominated by a process local to the subsolar point.

Several studies have addressed the combination of solar wind and IMF parameters that would yield optimal prediction of the following geomagnetic activity parametrized by geomagnetic auroral electrojet indices: The solar wind electric field (E_Y, equation (1)) gives the subsolar reconnection efficiency [*Burton et al.*, 1975; *Vasyliunas*, 1975]; the electric field parallel to the large-scale X line (E_{PAR}, equation (2)) accounts for the three-dimensional fields. The ϵ parameter (equation (3)) describes the Poynting flux incident at the magnetopause [*Akasofu*, 1981], while the universal coupling function ($d\Phi_{MP}/dt$, equation (4)) is proportional

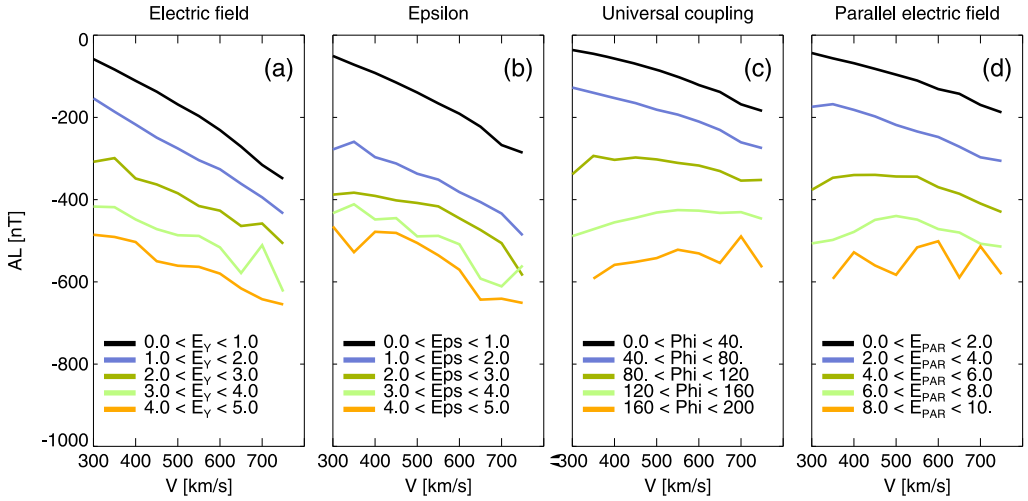

Figure 1. *AL* index as function of solar wind speed for five values of the driver function: (a) solar wind electric field E_Y in units of mV/m, (b) the ϵ parameter in units of 10^{11} W, (c) the universal coupling function $d\Phi_{MP}/dt = (V^2 B_T)^{2/3} \sin^{8/3}(\frac{\theta}{2})$ in units of $((m/s)^2 T)^{2/3}$, and (d) the parallel electric field along the large-scale X line E_{PAR} in units of mV/m.

to the rate at which magnetic flux is opened at the magnetopause [*Newell et al.*, 2007]. The formulations for all functions can be separated to a magnetic component and a component linear in solar wind speed:

$$E_Y = -VB_Z \tag{1}$$

$$E_{\mathrm{PAR}} = VB \sin\left(\frac{\theta}{2}\right) \tag{2}$$

$$\epsilon \propto VB^2 \sin^4\left(\frac{\theta}{2}\right) \tag{3}$$

$$\left(\frac{d\Phi_{\mathrm{MP}}}{dt}\right)^{3/4} \propto VB_T^{1/2} \sin^2\left(\frac{\theta}{2}\right) \tag{4}$$

where B is the magnetic field magnitude and $B_T = \sqrt{B_X^2 + B_Y^2}$ is the tangential component in the geocentric solar magnetospheric coordinate system.

Examination of the statistical response of the *AL* index to the solar wind driver functions shows that especially for typical solar wind conditions and rather low level of driving, none of the coupling functions perform very well. We use the OMNI 1 min database (http://spdf.gsfc.nasa.gov/), which provides upstream solar wind and IMF parameters propagated to the bow shock nose (see *King* [2005] for data processing and propagation methods). In order to account for the transfer time between the magnetopause and the ionosphere, we created 1 h sliding averages of the driver functions and the *AL* index. Figure 1 shows the *AL* response as a function of solar wind speed for five different values of the driver function. For all driver functions, for low level of driving, the *AL* activity is larger for higher solar wind speed. For solar wind electric field and the epsilon parameter, the same remains true for all levels of driving, while the effect is not present for higher driving when using the universal coupling function or electric field parallel to the large-scale X line.

In this paper, we return to the role of the solar wind speed in the energy transfer process by examining how the solar wind parameters change at the shock crossing and what the implications are for the conditions prevalent at the magnetopause. With this information, we reexamine the effects of the solar wind speed and the magnetic component on the *AL* activity.

2. Driver Parameters in the Magnetosheath

We use data from the Time History of Events and Macroscale Interactions During Substorms (THEMIS) mission [*Angelopoulos*, 2008] from the period 2007 to 2013. Magnetic field measurements are provided by the fluxgate magnetometer instrument [*Auster et al.*, 2008], whereas the plasma velocity, density, and pressure

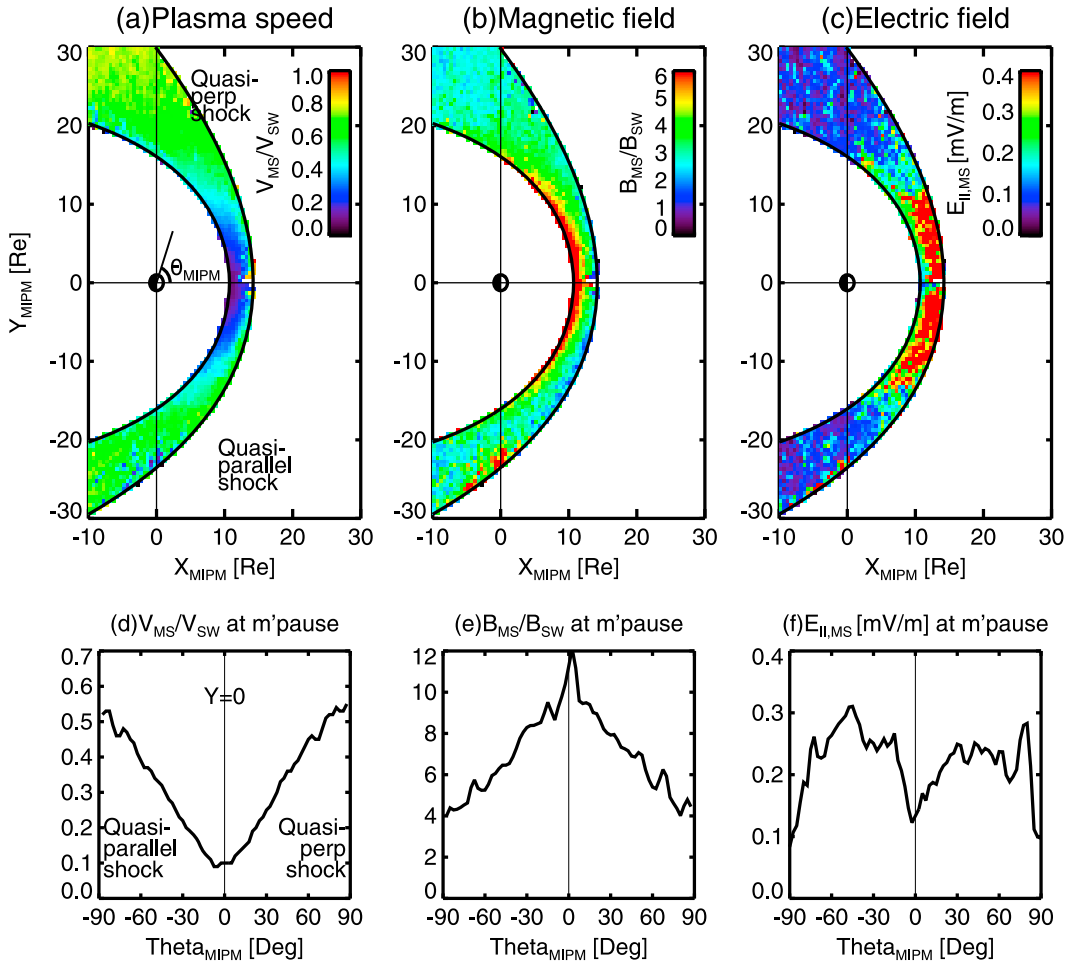

Figure 2. Magnetosheath plasma parameters in the MIPM frame of reference. (a) Plasma speed and (b) magnetic field magnitude scaled to the corresponding upstream solar wind values, and (c) electric field parallel to the magnetopause in mV/m. Magnetosheath plasma parameters averaged over values within 20% of the magnetosheath thickness closest to the magnetopause as a function of angle θ_{MIPM} from the X_{MIPM} direction. (d) Plasma speed and (e) magnetic field magnitude scaled to the corresponding upstream solar wind values, and (f) electric field parallel to the magnetopause in mV/m.

measurements come from the THEMIS onboard moments from the electrostatic analyzer instrument [*McFadden et al.*, 2008].

In order to analyze the magnetosheath statistical properties as a function of upstream solar wind conditions, we examine the THEMIS observations in the magnetosheath interplanetary medium (MIPM) reference frame [*Verigin et al.*, 2006]. In this frame the $\hat{e}_x$ axis is oriented antiparallel to the upstream solar wind flow, and the $\hat{e}_y$ axis is perpendicular to the $\hat{e}_x$ axis with the IMF vector in the $\hat{e}_x - \hat{e}_y$ plane. Thus, each point is rotated around the Sun-Earth line to the plane of the IMF, reducing the three-dimensional data set to a two-dimensional plane. In this representation, the quasi parallel shock is always on the "dawn" side, while the quasi perpendicular shock is on the "dusk" side. The radial fractional distance is measured from 0 at the magnetopause to 1 at the bow shock. The bow shock position is calculated from the model by *Verigin et al.* [2001] and the magnetopause position from the model by *Shue et al.* [1998]. This coordinate system organizes the THEMIS observations in relation to position relative to magnetopause and bow shock locations as well as the IMF Parker spiral orientation [*Dimmock and Nykyri*, 2013].

Figure 2 shows the magnetosheath plasma speed, magnetic field, and electric field magnitude scaled by corresponding upstream solar wind values. Figures 2a and 2b follow *Dimmock and Nykyri* [2013], who demonstrated the significant reduction of the solar wind speed and the strong compression of the magnetic field near the subsolar region. The values shown are scaled by the upstream values and thus reflect changes

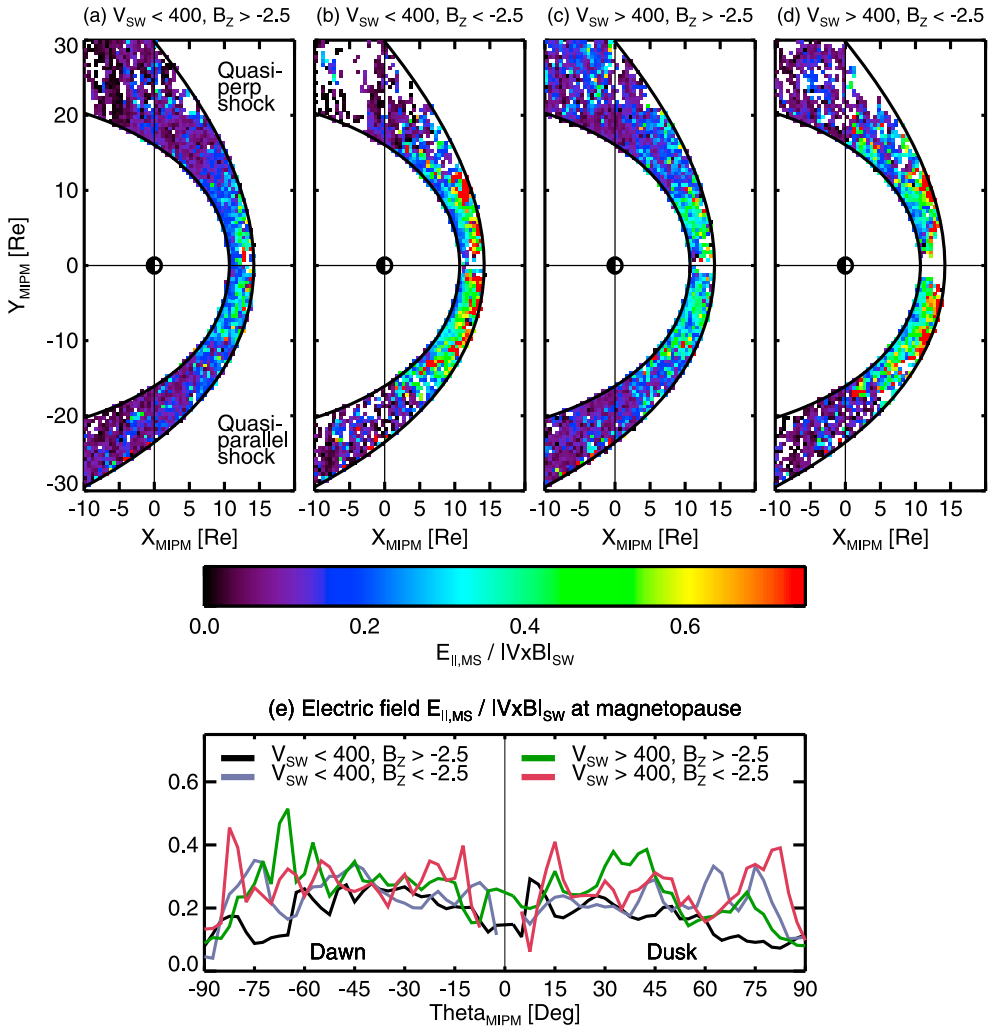

Figure 3. Magnetosheath electric field parallel component scaled to the upstream values. The data are divided into four subsets with (a) low driving $-2.5 < B_Z < 0$ nT and $V < 400$ km/s, intermediate driving with (b) $-20 B_Z < -2.5$ nT and $V < 400$ and (c) $-2.5 < B_Z < 0$ nT and $V > 400$, and (d) high driving $-20 < B_Z < -2.5$ nT and $V > 400$ km/s. (e) Magnetosheath electric field parallel component scaled to the upstream values averaged over values within 20% of the magnetosheath thickness closest to the magnetopause as a function of the θ_{MIPM} angle (in degrees). The average electric field magnitude in the solar wind is 0.26 mV/m.

from the upstream conditions. Figure 2c shows the electric field component parallel to the magnetopause $E_{||,MS} = (-\mathbf{V_{MS}} \times \mathbf{B_{MS}})_{||}$. The parallel component was computed by taking the component tangent to the model magnetopause at the location of the observation and shows the value of the electric field (in mV/m) not scaled by the upstream value. For typical solar wind values, the electric field is a few millivolts per meter (e.g., $B_Z = -2.5$ nT and $V_X = -400$ km/s produce $E_Y = 1$ mV/m). Figures 2d–2f show the values near the magnetopause obtained by computing the average value within 0–20% of the magnetosheath thickness.

Figure 2 clearly demonstrates that the strong reduction in solar wind speed reduces the parallel component of the electric field to only a small fraction of the upstream driving electric field. Furthermore, the electric field is larger in the quasi parallel side (by about 15%), reducing toward the flanks as the magnetic field becomes draped and increasingly parallel to the plasma flow. This would indicate that the most favorable conditions for plasma and energy entry would be at the quasi parallel magnetopause sunward of the terminator. Note that antiparallel fields favorable for reconnection are largely generated by the B_Z component of the IMF. However, as the field becomes draped, the B_Y and B_X components add to the electric field component along the large-scale neutral line away from the subsolar region.

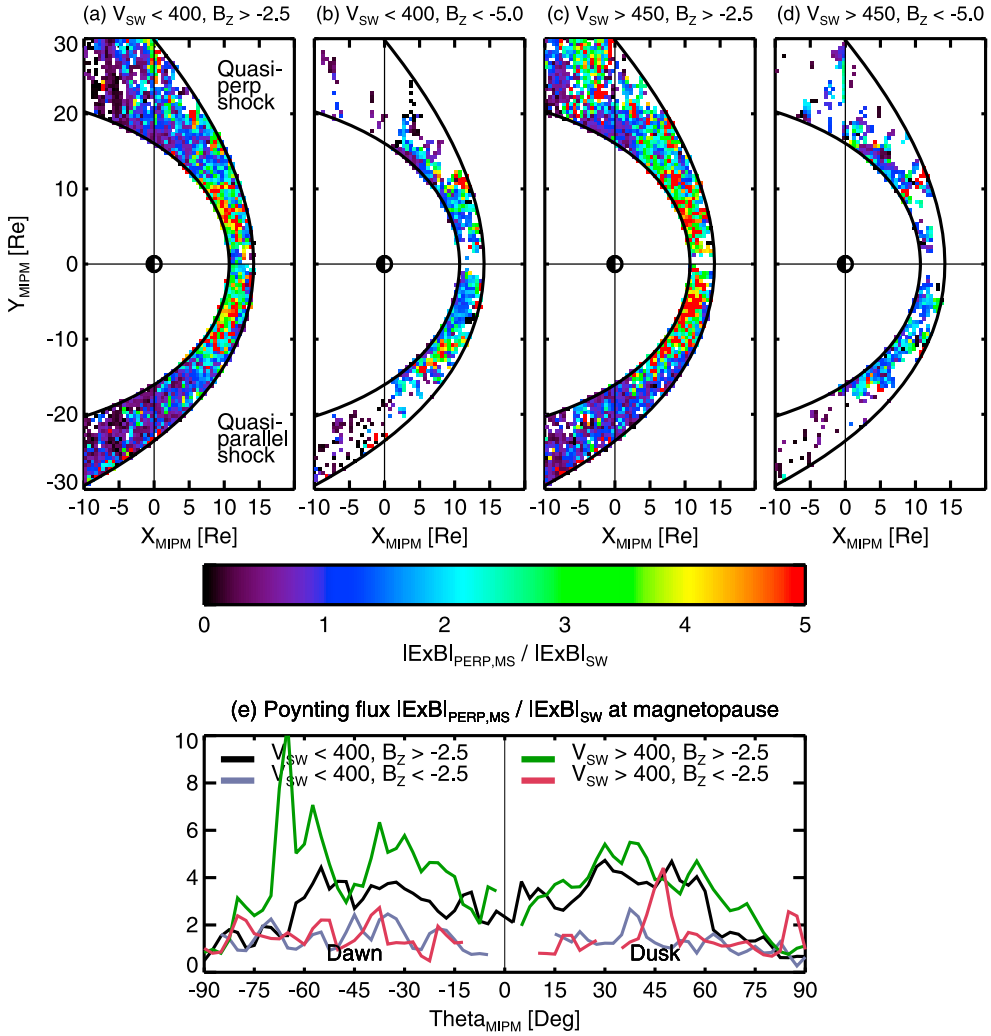

Figure 4. Magnetosheath Poynting flux component normal to the magnetopause $S_\perp$ scaled to the upstream values. The data are divided into four subsets with (a) low driving $-2.5 < B_Z < 0$ nT and $V < 400$ km/s, (b) intermediate driving $-20 B_Z < -5.0$ nT and $V < 400$ and (c) $-2.5 < B_Z < 0$ nT and $V > 450$, and (d) high driving $-20 < B_Z < -5.0$ nT and $V > 450$ km/s. (e) Magnetosheath perpendicular Poynting flux $S_\perp$ scaled to the upstream values averaged over values within 20% of the magnetosheath thickness closest to the magnetopause as a function of the θ_{MIPM} angle (in degrees). The average values near the magnetopause are 9.2, 35.9, 12.4, and 66.3 $\mu W/m^2$ for the four data sets, respectively.

Considering the different behavior of B and V across the bow shock, we further examine the electric field for different solar wind and IMF parameters. We concentrate here on southward IMF conditions. We examine separately cases with weakly southward IMF ($-2.5 < B_Z < 0$ nT) and strongly southward IMF ($B_Z < -2.5$ nT). Furthermore, we separate the data set into slow solar wind flow ($V < 400$ km/s) and fast solar wind flow ($V > 400$ km/s). Figure 3 shows the electric field parallel component values in the magnetosheath scaled by the upstream solar wind electric field magnitude. Figure 3a shows the weak driving conditions under which the solar wind speed is low, and IMF B_Z is only moderately negative. Figure 3d shows the opposite case with high solar wind speed and strongly negative IMF B_Z. The number of observations in each category is (a) 131,406; (b) 59,725; (c) 104,915; and (d) 39,327.

While Figures 3a–3d show in the large scale a similar pattern, there are also differences. The electric field tends to be stronger close to the shock and decreases toward the magnetopause. Strongly negative IMF B_Z creates higher electric field values close to the shock (Figures 3b and 3d). At the magnetopause, the most conditions that generate the largest electric fields involve high solar wind speed (Figures 3c and 3d, and red and green curves in Figure 3e). Furthermore, the electric field parallel to the magnetopause maximizes away from the subsolar region for all conditions.

Earlier studies using MHD simulations [e.g., *Palmroth et al.*, 2006] show that the vast majority of the energy are transferred from the solar wind to the magnetosphere in the form of the Poynting flux $\mathbf{S} = \mathbf{E} \times \mathbf{B}/\mu_0$. To investigate the energy available at the magnetopause, we compute the component of the Poynting vector perpendicular to the magnetopause, again scaling the values with the upstream solar wind values. Figure 4 shows $(\mathbf{E} \times \mathbf{B})_\perp / \mid \mathbf{E} \times \mathbf{B} \mid_{SW}$ by computing the perpendicular directions similar to the electric field using the model magnetopause normal. From this plot it is evident that the most efficient energy transfer takes place slightly away from the subsolar region, about 45° from the subsolar direction. Furthermore, the energy transfer is more efficient on the quasi parallel shock side and again most efficient when the solar wind speed is high and the IMF B_Z is only moderately negative. Note that the absolute values of the energy transfer for low driving and high driving are very different, as the curves in Figure 3e are scaled by the upstream values. Note also that, in order to better distinguish the different driving conditions, we have in this case limited the fast solar wind values to speeds above 450 km/s and strongly negative IMF B_Z to values $B_Z < -5.0$ nT.

In conclusion, the solar wind electric field is modified as the solar wind crosses the bow shock. The combined effect of the deflection of the flow along the magnetospheric boundary and the compression of the magnetic field lead to strongest electric field parallel to the magnetopause in the quasi parallel shock side of the dayside magnetopause. The most likely positions for energy transfer reside in the magnetopause region sunward of the terminator line but away from the subsolar region. The energy is transferred in the form of Poynting flux—the Poynting vector component perpendicular to the magnetopause is an indicator of the regions of energy transfer. As shown in Figure 4, the perpendicular Poynting flux at the magnetopause maximizes in the magnetosheath (relative to the upstream values) when the solar wind speed is high and the magnetic field is only moderately negative. Thus, high solar wind speed under relatively average driving provides magnetopause conditions that are most favorable for energy and plasma entry into the magnetosphere.

3. Discussion

In this paper we show that typically used solar wind driver functions do not give consistent results for low and high solar wind speed: for similar driver values, high solar wind speed conditions produce higher activity than a combination where the magnetic field component is larger and the solar wind speed is correspondingly lower (Figure 1). Using the THEMIS measurements tagged with solar wind driver properties, we show that the electric field is relatively uniform in the magnetosheath near the magnetopause from one flank to the other but that the electric field transfer from the upstream undisturbed solar wind to the magnetosheath near the magnetopause is most efficient when the solar wind speed is high and the IMF B_Z is only moderately negative (Figure 3). Similarly, the Poynting flux normal to the magnetopause is highest when the solar wind speed is high (Figure 4). The Poynting flux transfer is lower at the subsolar region and increases toward the flanks, before decreasing toward the terminator and beyond. We therefore conclude that the effect of the high solar wind speed is caused by the combination of the magnetic field and plasma transport properties across the bow shock and magnetosheath (see Figure 2).

Figures 3 and 4 provide an explanation of the result in Figure 1: As the electric field determining the reconnection efficiency is a combination of speed and magnetic field, and as these parameters change independently depending on the location, the reconnection driving electric field at the magnetopause is not a simple function of the solar wind E_Y but favors conditions with high solar wind speed and moderately negative B_Z.

In many statistical analyses, strong driving conditions dominate the correlations between the driver and response. Thus, for higher levels of driving, the driver functions perform quite well [e.g., *Newell et al.*, 2007], which makes them valuable for prediction of space weather events. However, for the sake of understanding the details of the coupling processes, it is important to consider also the average and low levels of driving and geomagnetic activity. This study sheds light on how the bow shock conditions and the magnetosheath processes lead to differences in high and low solar wind speed cases as well as weakly and strongly negative IMF B_Z cases.

Sergeev et al. [2014] suggest that a key parameter for driving ionospheric activity, but missing in earlier analyses, is $\sqrt{(T)}/N$ in the plasma sheet. The plasma sheet temperature (T) and density (N) affect the field-aligned acceleration and precipitating particle flux, ionospheric conductivity, and the field-aligned current intensity. As high solar wind speed leads to low density and high temperature (hot tenuous plasma sheet), while low solar wind speed produces high density and low temperature (cold dense plasma sheet) [*Borovsky et al.*, 1998;

Wang et al., 2007]; this result is consistent with ours predicting higher activity for high solar wind speed. Thus, in addition to the variations through the bow shock and magnetosheath, there may be a second effect within the magnetosphere that operates in the same direction of increasing activity for higher solar wind speeds.

A topic deserving further study is the energy entry not related to large-scale magnetic reconnection. These "viscous interaction" processes [*Axford and Hines*, 1961] may include a variety of diffusive processes and/or boundary instabilities, most notably the Kelvin-Helmholtz instability (KHI) [e.g., *Nykyri and Otto*, 2001]. In a recent study, *Dimmock et al.* [2014] show that high solar wind speed drives higher level of fluctuations in the magnetosheath, regardless of the level of fluctuations in the solar wind. Furthermore, two-dimensional MHD simulations can be used to show that the KHI is enhanced by an increased level of fluctuations in the magnetosheath. Thus, higher fluctuations in the magnetosheath will lead to enhanced energy and plasma transfer by KHI through the magnetopause.

The probability distribution function of the *AL* index is highly non-Gaussian in most situations; the exception being strongly southward IMF conditions. Therefore, it is important to note that the *AL* mean (or median) is not a good parameter to characterize the response to a given driver. Furthermore, we propose a bimodal response of the *AL* index to strongly northward and southward driving. This may indicate that the solar wind driver under southward (reconnection-dominated) and northward (viscous interaction dominated) conditions will have different functional dependences on the solar wind parameters.

4. Conclusions

1. Analysis of the *AL* response to different solar wind drivers (E_Y, E_{PAR}, ϵ, $d\Phi_{MP}/dt$) shows that the result depends on the combination of the magnetic component (*B* magnitude and orientation) and solar wind speed such that higher speed produces higher *AL* activity for the same value of the driver function.
2. THEMIS results show that the electric field parallel to the magnetopause maximizes at the quasi parallel (dawn) flank. The magnetopause field compared to the upstream solar wind conditions is largest for cases when the solar wind speed is high and the IMF B_Z is only moderately negative.
3. The Poynting flux normal to the magnetopause maximizes at the dawn flank sunward of the terminator. Similarly to the electric field, the energy input compared to the upstream conditions is largest for high solar wind speed and moderately negative for B_Z.

Acknowledgments
This work was funded by the Academy of Finland through grant 267073/2013. The THEMIS data are available at http://themis.ssl.berkeley.edu/index.shtml and the OMNI data at http://omniweb.gsfc.nasa.gov both free of charge.

The Editor thanks Joseph Borovsky and an anonymous reviewer for their assistance in evaluating this paper.

References

Akasofu, S.-I. (1981), Energy coupling between the solar wind and the magnetosphere, *Space Sci. Rev.*, *28*, 121–190.
Angelopoulos, V. (2008), The THEMIS mission, *Space Sci. Rev.*, *141*(1–4), 5–34.
Auster, H. U., et al. (2008), The THEMIS fluxgate magnetometer, *Space Sci. Rev.*, *141*(1–4), 235–264.
Axford, W. I., and C. O. Hines (1961), A unifying theory of high-latitude geophysical phenomena and geomagnetic storms, *Canadian J. Phys.*, *39*, 1433–1464.
Baker, D. N., T. I. Pulkkinen, V. Angelopoulos, W. Baumjohann, and R. L. McPherron (1996), Neutral line model of substorms: Past results and present view, *J. Geophys. Res.*, *101*, 12,975–13,010, doi:10.1029/95JA03753.
Borovsky, J. E., M. F. Thomsen, and R. C. Elphic (1998), The driving of the plasma sheet by the solar wind, *J. Geophys. Res.*, *103*(A8), 17,617–17,639, doi:10.1029/97JA02986.
Burton, R. K., R. L. McPherron, and C. T. Russell (1975), An empirical relationship between interplanetary conditions and Dst, *J. Geophys. Res.*, *80*, 4204–4214.
Cowley, S. W. H. (1982), The causes of convection in the Earth's magnetosphere: A review of developments during the IMS, *Rev. Geophys.*, *20*(3), 531–565, doi:10.1029/RG020i003p00531.
Dimmock, A. P., and K. Nykyri (2013), The statistical mapping of magnetosheath plasma properties based on THEMIS measurements in the magnetosheath interplanetary medium reference frame, *J. Geophys. Res. Space Physics*, *118*, 4963–4976, doi:10.1002/jgra.50465.
Dimmock, A. P., K. Nykyri, and T. I. Pulkkinen (2014), A statistical study of magnetic field fluctuations in the dayside magnetosheath and their dependence on upstream solar wind conditions, *J. Geophys. Res. Space Physics*, *119*, 6231–6248, doi:10.1002/2014JA020009.
Dungey, J. (1961), Interplanetary magnetic field and the auroral zones, *Phys. Rev. Lett.*, *6*(2), 47–48.
Hones, E. W. J. (1979), Plasma flow in the magnetotail and its implications for substorm theories, in *Dynamics of the Magnetosphere*, edited by A. T. Y. Lui, Y. Kamide, and G. Consolini, pp. 545–562, D. Reidel, Dordrecht, Netherlands.
Janhunen, P., M. Palmroth, T. Laitinen, I. Honkonen, L. Juusola, G. Facskó, and T. I. Pulkkinen (2012), The GUMICS-4 global MHD magnetosphere-ionosphere coupling simulation, *J. Atmos. Sol. Terr. Phys.*, *80*(C), 48–59.
Kepko, L., et al. (2014), Substorm current wedge revisited, *Space Sci. Rev.*, *124*, doi:10.1007/s11214-014-0124-9.
King, J. H. (2005), Solar wind spatial scales in and comparisons of hourly Wind and ACE plasma and magnetic field data, *J. Geophys. Res.*, *110*, A02104, doi:10.1029/2004JA010649.
Laitinen, T. V., M. Palmroth, T. I. Pulkkinen, P. Janhunen, and H. E. J. Koskinen (2007), Continuous reconnection line and pressure-dependent energy conversion on the magnetopause in a global MHD model, *J. Geophys. Res.*, *112*, A11201, doi:10.1029/2007JA012352.
Lyon, J. G., J. A. Fedder, and C. M. Mobarry (2004), The Lyon-Fedder-Mobarry (LFM) global MHD magnetospheric simulation code, *J. Atmos. Sol. Terr. Phys.*, *66*(15–16), 1333–1350.
McFadden, J. P., C. W. Carlson, D. Larson, M. Ludlam, R. Abiad, B. Elliott, P. Turin, M. Marckwordt, and V. Angelopoulos (2008), The THEMIS ESA plasma instrument and in-flight calibration, *Space Sci. Rev.*, *141*(1–4), 277–302.

Newell, P. T., T. Sotirelis, K. LIOU, C. I. Meng, and F. J. Rich (2007), A nearly universal solar wind-magnetosphere coupling function inferred from 10 magnetospheric state variables, *J. Geophys. Res.*, *112*, A01206, doi:10.1029/2006JA012015.

Nishida, A., T. Mukai, T. Yamamoto, Y. Saito, and S. Kokubun (1996), Magnetotail convection in geomagnetically active times—1. Distance to the neutral lines, *J. Geomagn. Geoelectr.*, *48*, 489–501.

Nykyri, K., and A. Otto (2001), Plasma transport at the magnetospheric boundary due to reconnection in Kelvin-Helmholtz vortices, *Geophys. Res. Lett.*, *28*(18), 3565–3568, doi:10.1029/2001GL013239.

Palmroth, M., T. Laitinen, and T. I. Pulkkinen (2006), Magnetopause energy and mass transfer: Results from a global MHD simulation, *Ann. Geophys.*, *24*, 3467–3480.

Pudovkin, M. I., V. S. Semenov, M. F. Heyn, and H. K. Biernat (1986), Implications of the stagnation line model for energy input through the dayside magnetopause, *Geophys. Res. Lett.*, *13*(3), 213–216, doi:10.1029/GL013i003p00213.

Pulkkinen, T. I., M. Palmroth, H. E. J. Koskinen, T. V. Laitinen, C. C. Goodrich, V. G. Merkin, and J. G. Lyon (2010), Magnetospheric modes and solar wind energy coupling efficiency, *J. Geophys. Res.*, *115*, A03207, doi:10.1029/2009JA014737.

Sergeev, V. A., D. A. Sormakov, and V. Angelopoulos (2014), A missing variable in solar wind-magnetosphere-ionosphere coupling studies, *Geophys. Res. Lett.*, *41*, 8215–8220, doi:10.1002/2014GL062271.

Shue, J.-H., J. K. Chao, H. C. Fu, C. T. Russell, P. Song, K. K. Khurana, and H. J. Singer (1998), Magnetopause location under extreme solar wind conditions, *J. Geophys. Res.*, *103*, 17,691–17,700, doi:10.1029/98JA01103.

Sonnerup, B. U. O. (1974), Magnetopause reconnection rate, *J. Geophys. Res.*, *10*, 1546–1549.

Vasyliunas, V. (1975), Theoretical models of magnetic field line merging, *Rev. Geophys.*, *13*, 303–336.

Verigin, M. I., et al. (2001), Analysis of the 3-D shape of the terrestrial bow shock by Interball/Magion 4 observations, *Adv. Space Res.*, *28*(6), 857–862, doi:10.1016/S0273-1177(01)00502-6.

Verigin, M. I., M. Tatrallyay, G. Erdos, and G. A. Kotova (2006), Magnetosheath interplanetary medium reference frame: Application for a statistical study of mirror type waves in the terrestrial plasma environment, *Adv. Space Res.*, *37*, 515–521, doi:10.1016/j.asr. 2005.03.042.

Wang, C.-P., L. R. Lyons, T. Nagai, J. M. Weygand, and R. W. McEntire (2007), Sources, transport, and distributions of plasma sheet ions and electrons and dependences on interplanetary parameters under northward interplanetary magnetic field, *J. Geophys. Res.*, *112*, A10224, doi:10.1029/2007JA012522.

Yeh, T. (1976), Day side reconnection between a dipolar geomagnetic field and a uniform interplanetary field, *J. Geophys. Res.*, *81*(13), 2140–2144, doi:10.1029/JA081i013p02140.